International Journal of Heat and Mass Transfer 174 (2021) 121343

Contents lists available at ScienceDirect

International Journal of Heat and Mass Transfer

journal homepage: www.elsevier.com/locate/hmt

A parallelizable mesh-free approach for simulation of heat conduction in ferromagnetic particulate materials under magnetic field effect

Reza Bahadori[a,*], Hector Gutierrez[a], Shahin Shafiee[b]

[a] Florida Institute of Technology, Melbourne, FL 32901 USA
[b] Prairie View A&M University, USA

ARTICLE INFO

Article history:
Received 8 September 2020
Revised 31 March 2021
Accepted 6 April 2021

Keywords:
Heat transfer enhancement
Particle beds
Porous media
Magnetic field
Mesh-free
Monte-Carlo

ABSTRACT

A novel mesh-free approach has been developed to solve the conduction heat transfer equations in a particulate bed domain of ferromagnetic powder with and without magnetic field effect. The proposed method is based on a probabilistic approach to defining various configurations of energy transfer paths around an arbitrary particle called "local packed element", and results are compared with experimental data. Furthermore, a Monte-Carlo approach is used to calculate the magnetic field of a permanent magnet with an arbitrary shape on any arbitrary point around it, and the outcome is also compared against measurements. In both cases, the proposed mesh-free method shows excellent agreement with available empirical results. The proposed method is then used to model the effect of an external magnetic field in the conductive heat transfer in a particulate bed of ferromagnetic powder. It is concluded that the presence of a magnetic field increases thermal diffusion in ferromagnetic powder bed domains by increasing thermal conductivity.

1. Introduction

Porous and particulate materials are used in various important engineering and scientific applications. Heat transfer in such domains is a main design concern in many of these applications. Electrical devices [1], 3D metal printing [2,3] and selective laser sintering [4,5], solid fuel-cells [6,7], thermal barrier coating [8–10], and fixed and moving bed heat exchangers [11,12] are examples of industrial applications of particulate materials which modeling of heat transfer is one the essential design challenges today. To expand it more, there is great interest in both academy and industry to investigate the use of particulate beds of metal hydrides for applications such as heat pumps [13,14]. Particle bed reactors are being designed for space nuclear applications [15]. As mentioned, thermal management in most of these applications is critical in the design process. Simulation of heat transfer in particulate beds requires taking into consideration the size and shape of the particles, volume fraction, porosity, interfacial thermal resistance and the configuration of particle assembly. Several numerical methods have been used to model the heat transfer behavior of particle beds. Finite Element Methods (FEM) are particularly well established for the simulation of the heat transfer problem in particle beds. In microscale (a simulation domain including a small number of particles) a FEM model of a particle bed may include most relevant details of the particle configuration into account [16–19]. On the other hand, the simulation of macroscale problems, including previously considered intricate geometric details in the calculation, is computationally prohibitive for FEM. In other words, to model a particle bed with a significant level of geometric fidelity using finite element methods is computationally very intensive and possibly impractical, since the number of elements required to realistically represent the geometry of particle bed configurations in macroscale problems is very large. In FEM simulations, a large number of elements yields a large stiffness matrix that needs to be inverted at each time step, which leads to a significant increase of the computational burden as the number of elements increases. The conventional approach to deal with this issue when using FEM models to develop macroscale simulations is based on the use of "effective" parameters to model the average behavior of particle beds. That is, the details of possible geometric configurations are not modeled, and instead "equivalent parameters" based on particle size, configuration, volume fraction, thermal properties of materials, etc., are used [20–24]. Such approximations, when using FEM models to analyze macroscale problems, may lead to significant loss of fidelity. In this context, the boundary element method seems to be a better fit technique as discretization only occurs at the boundary of the particle rather than inside the whole particle [25–27]. Hybrid approaches are developed to improve the

* Corresponding author.
E-mail addresses: rbahadori2013@my.fit.edu (R. Bahadori), hgutier@fit.edu (H. Gutierrez), shshafiee@pvamu.edu (S. Shafiee).

https://doi.org/10.1016/j.ijheatmasstransfer.2021.121343
0017-9310/

homogenization and volume averaging. Polansky et.al combined 2D and 3D porous media modeling with a resistive network model to estimate the effective conductivity [28].

When modeling particle beds, the discrete element method (DEM) aims at connecting the microscale parameters of particles such as particle size, surface to volume ratio, surface roughness, porosity, and shape to the macroscale properties of the packed particle bed, such as thermal conductivity, bulk porosity, angle of repose, cohesion, etc., by using molecular dynamics governing equations. Several surveys can be found describing various approaches to undertake heat transfer in particulate beds using DEM or combined DEM-FEM approaches [29–34]. The main difficulty when modeling a system with millions or billions of particles lies in finding where the nearest neighbors are: the model needs to represent how particles with different sizes and shapes pack. In the current state of the art, deterministic pre-location of particles in a lattice (including fine particles in a porous bed) is typically implemented using Voronoi tessellation in DEM, or Monte-Carlo techniques [35,36].

Randomness is an important characteristic of the distribution of particles in a particle bed. The size, shape, material, and location of each particle can be realistically described by appropriate distribution functions within specified ranges of the particle's properties. Probabilistic methods like Monte-Carlo have been used to address heat transfer solution in numerous studies [37–39]. They are strong candidates to solve boundary and initial value problems in particle beds since they inherently incorporate the random nature of the relevant physical parameters involved. Recent studies in both two and three-dimensional systems [40,41] have used Monte-Carlo based probabilistic approaches combined with analytical solutions in polar and spherical coordinates to solve the steady-state and transient heat conduction problem in composite materials. This paper describes an adaption of the latter parallelizable method that uses a probabilistic approach to provide a high-fidelity model of particle configuration as relevant to the solution of the heat transfer problem, while addressing the aforementioned limitations in the state of the art macroscale models based on FEM and DEM.

2. Formulations

2.1. Heat transfer

The "Effective Floating Volume" (EFV) [42] is a novel approach proposed by Bahadori et al. to solve transient heat conduction problems in multi-scale systems, i.e., systems where small and large dimensions need to be considered to properly describe the system's geometry. Important examples of multi-scale systems are physical domains with thin layers of materials that have significant effect in the physics being considered, such as thermal or electrical insulators in electrical machines or the layers in a superconducting material. When using EFV to solve heat transfer equations, the temperature at the center point of a spherical element is calculated using Eq. (1):

$$T_C = \frac{\int_0^{2\pi}\int_0^{\pi}\frac{T_1(r,\theta,\varphi)+\sum_{m=2}^{M} dT_m(r,\theta,\varphi)}{\int_0^R \frac{dr'}{\sin(\theta)r'^2\alpha(r',\theta,\varphi,T)}}d\theta d\varphi}{\int_0^{2\pi}\int_0^{\pi}\frac{1}{\int_0^R \frac{dr'}{r'^2\sin(\theta)\alpha(r',\theta,\varphi,T)}}d\theta d\varphi} \tag{1}$$

where r, θ and φ are radius, elevation, and azimuth in spherical coordinates, α is thermal diffusivity and T the corresponding temperature. The EFV method is based on the numerical integration of the energy transfer through paths starting at the boundary of a spherical element and ending at its center, where $dT_m = T_m - T_{m-1},\ m = 2,\ 3, \ldots, M$ denotes the temperature difference at the acquisition points numbered from the center to the boundary. This formulation takes into account the initial condition, boundary condition, and heat source effect at every point in the sphere, and converts their combined effects into temperature at the corresponding acquisition points; numerical integration is then used to calculate the impact of all points within the sphere on the temperature at the center point T_C. In this paper, the EFV method is adapted to model heat conduction in particle beds.

When modeling heat conduction in particle beds, thermal energy is transferred from one particle to the adjacent ones; heat flow and thermal contact resistance are the main parameters in the analytical derivation of the energy transfer through each path. The other path of energy transfer is through conduction by the interstitial gas trapped in the porous cavities between particles, and radiation heat transfer is neglected. Heat transfer in micro contacts is modeled by conduction through the gas in the micro gaps and conduction trough the solid points of contact. Bahrami et al. [21] developed formulations for the effective thermal resistance in rough spherical packed beds. From this method, one can develop a formulation for ellipsoids with arbitrary radii, since ellipsoids are good approximations for particle shapes. Fig. 1 depicts the different types of heat flow between two particles in two and three-dimensional approximations. The equivalent system shown in Fig. 1 can be calculated by Eq. (2):

$$\mathrm{P} = \left[\frac{1}{(1/\mathrm{P}_s + 1/\mathrm{P}_g)^{-1} + \mathrm{P}_L} + \frac{1}{\mathrm{P}_G}\right]^{-1} \tag{2}$$

where P_s is the thermal resistance in the micro contacts, P_g the thermal resistance of the gas trapped between micro contacts, P_L the constriction thermal resistance in the particles, and P_G the thermal resistance of the gas between particles.

Fig. 1 shows the layout of two particles randomly placed in contact. In the two-dimensional case, the distances $r_{c,1}$ and $r_{c,2}$ can be calculated using Eqs. (3) and (4). The path length of heat transfer between two center points is $L = r_{c,1} + r_{c,2}$. Starting from particle 1, ω defines the angle that particle two comes in contact with particle one with respect to the global coordinate system. The procedure repeats for the next particle to eventually form a path for conductive energy transfer from boundary to sink. $r_{s,1}$, $r_{s,2}$, $r_{b,1}$, and $r_{b,2}$, are possible values for major (b) and minor (s) radii for particles 1 and 2.

$$r_{c,1} = \left[\frac{1}{r_{s,1}^2}\cos^2(\omega) + \frac{1}{r_{b,1}^2}\sin^2(\omega)\right]^{-1/2} \tag{3}$$

$$r_{c,2} = \left[\frac{1}{r_{s,2}^2}\cos^2(\omega+\pi) + \frac{1}{r_{b,2}^2}\sin^2(\omega+\pi)\right]^{-1/2} \tag{4}$$

The Monte-Carlo method can be used to generate a random distribution of the above angles and dimensions. Eqs. (5)–(7) represent the corresponding probability functions: probability distributions of the particles' size, shape, and orientations within specified ranges.

$$r_s = r_{s,max} - [(r_{s,max} - r_{s,min})RN] \tag{5}$$

$$r_b = r_{b,max} - \left[\left(r_{b,max} - r_{b,min}\right)RN\right] \tag{6}$$

$$\omega = 2\pi\,(RN) \tag{7}$$

where RN stands for a uniformly generated random number between 0 and 1. RN numbers are generated separately for each of the Eqs. (5)–(7). r_s and r_b are possible values for the small and big radius of the ellipsoid in the two-dimensional case, respectively; these radii are defined within ranges denoted by the intervals $[min, max]$. To minimize the particle overlap, parameters are set in the code to propagate the paths in the first layer around the center particle by a multiple order of 6 in 2D and 12 in 3D, then they branch in the next layers. (i.e., energy packets share the same

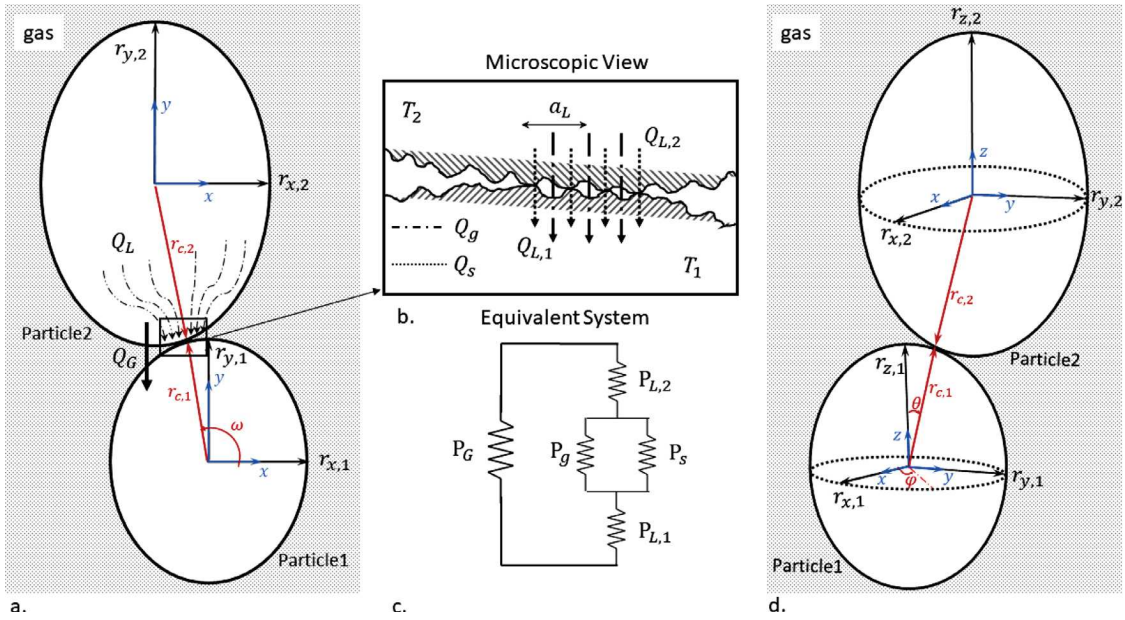

Fig. 1. Heat flow and thermal resistance between ellipsoidal particles with rough contact Area. (a) Two-dimensional case and relevant geometric parameters, and heat flow Q_g (b) microscopic view of thermal contact heat flow, (c) equivalent thermal resistance, (d) three-dimensional case: geometric parameters and heat flow.

path when they get closer to the center). Similarly, in the three-dimensional case, contact radii $r_{c,1}$ and $r_{c,2}$ can be calculated using Eqs. (8) and (9) and the heat transfer path length is $L = r_{c,1} + r_{c,2}$.

$$r_{c,1} = \left[\frac{1}{r_{s,1}^2}\sin^2(\theta)\cos^2(\varphi) + \frac{1}{r_{m,1}^2}\sin^2(\theta)\sin^2(\varphi) + \frac{1}{r_{b,1}^2}\cos^2(\theta)\right]^{-1/2} \tag{8}$$

$$r_{c,2} = \left[\frac{1}{r_{s,1}^2}\sin^2(\theta+\pi)\cos^2(\varphi+\pi) + \frac{1}{r_{m,1}^2}\sin^2(\theta+\pi)\sin^2(\varphi+\pi) + \frac{1}{r_{b,1}^2}\cos^2(\theta+\pi)\right]^{-1/2} \tag{9}$$

The geometric coordinates θ and φ are the elevation and azimuth angles for each particle's orientation in the global coordinate system, and ϑ and ψ are the elevation and azimuth angles that define the contact orientation of particle two with respect to particle one. In the three-dimensional case, the ellipsoidal volume is specified by small, medium and big radii noted as by r_s, r_m and r_b, respectively. Eqs. (10)–(14) are used to determine each geometric parameter value in its specified range $[min, max]$:

$$r_s = r_{s,max} - [(r_{s,max} - r_{s,min})RN] \tag{10}$$

$$r_m = r_{m,max} - [(r_{m,max} - r_{m,min})RN] \tag{11}$$

$$r_b = r_{b,max} - \left[\left(r_{b,max} - r_{b,min}\right)RN\right] \tag{12}$$

$$\theta = cos^{-1}(1 - 2RN) \tag{13}$$

$$\varphi = 2\pi\,(RN) \tag{14}$$

Fig. 2 illustrates a Monte-Carlo distribution of energy transfer paths in a three-dimensional domain. Each of the path distributions shown in Figs. 2 and 4 have shapes and orientations based on the random variables defined by Eqs. (3)–(14). The temperature in the center particle can be calculated using Eq. (1) and information of temperature from previous step and thermal resistivity from energy transfer path configuration. One can generate a bank of path

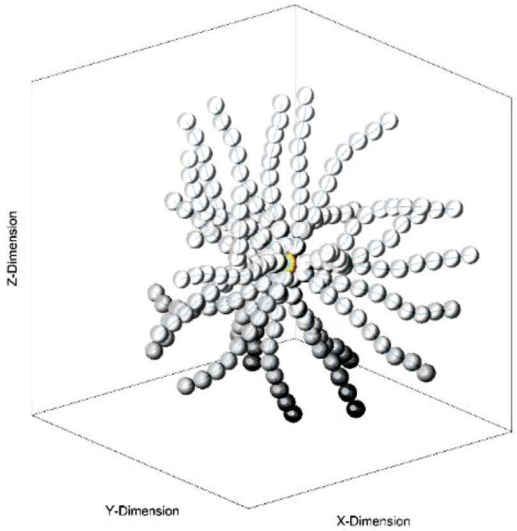

Fig. 2. Three-dimensional Monte-Carlo distribution of thermal energy transfer by random paths to the center point of a spherical element.

distributions and randomly call one of them to calculate the temperature at each desired point in the geometry. Eq. (15) is used to calculate the thermal resistance P_L experienced by each particle [21]:

$$P_L = \frac{1}{2k_s a_L} \tag{15}$$

where $k_s = 2k_1k_2/(k_1 + k_2)$ is the equivalent thermal conductivity of two contacting particles, and a_L the radius of macro contact as defined by Eq. (16) [43]:

$$a_L = \left(\frac{3r^*F}{4E^*}\right)^{1/3} \tag{16}$$

where $r^* = (1/r_{c,1} + 1/r_{c,2})^{-1}$, and $E^* = [(1 - \nu_1{}^2)/E_1 + (1 - \nu_2{}^2)/E_2]^{-1}$ is the equivalent modulus of elasticity calculated from the corresponding moduli of elasticity E_i and poison ratio ν_i of particles 1 and 2. The thermal contact resistance P_s can be

Table 1
Coefficients of the inverse probability function for Eq. (20) and (21).

	D_1	D_2	D_3	D_4
0.0-0.1	0.079578	0.079621	0.058919	0.048997
0.1-0.3	0.079515	0.081077	0.048261	0.074542
0.3-0.6	0.070722	0.150740	-0.13699	0.240830

obtained from the formulation developed in [44]:

$$P_s = \frac{0.565H^*(\sigma/m)}{k_s F} \tag{17}$$

where F is the contact force acting on the particle, $H^* = c_1(\sigma'/m)^{c_2}$, $\sigma' = \sigma/\sigma_0$, $\sigma = \sqrt{\sigma_1^2 + \sigma_2^2}$ is the combined roughness of two particles in contact, and $\sigma_0 = 1\ \mu m$. The surface slope is defined as $m = \sqrt{m_1^2 + m_2^2}$, and each surface slope is calculated based on its corresponding roughness: $m_p = 0.152\sigma_p^{0.4}$, $p = 1,\ 2$ [21]. c_1 and c_2 are defined in Eqs. (18) and (19), where $k = H_B/H_{BGM}$, H_B is the Brinell hardness of the bulk material (in *GPa*) and $H_{BGM} = 3.178\ GPa$.

$$c_1 = H_{BGM}\left(4.0 - 5.77k + 4.0k^2 - 0.61k^3\right) \tag{18}$$

$$c_2 = -0.57 + 0.82k - 0.41k^2 + 0.06k^3 \tag{19}$$

Heat transfer in micro gaps (P_g) and macro gaps (P_G) are neglected in this study, and the relations to calculate them are shown in [21].

Eqs. (20) and (21) provide the relationship between time τ and the corresponding distance r the energy can travel [41]. Having $= \sum_{i=1}^{N} L_i$, $L = r_{c,1} + r_{c,2}$, and the equivalent thermal conductivity from reciprocal of Eq. (2), the required time τ for an energy particle to travel the distance r can be calculated as:

$$\frac{\alpha\tau}{r^2} = D_1 + D_2(RN_3) + D_3(RN_3)^2 + D_4(RN_3)^3 RN3 < 0.6 \tag{20}$$

$$\frac{\alpha\tau}{r^2} = -0.10132In[0.5(1 - RN_3)]RN3 \geq 0.6 \tag{21}$$

Conversely, having the step time, one can trace the sequence of randomly distributed particles along the energy transfer path and reconstruct the sequence to the point that the required time is approximately equal to the step time τ. Table 1 shows the values of the coefficients in Eqs. (20) and (21).

2.2. Probabilistic model of magnetic field

To enhance thermal conduction in a particle bed of ferromagnetic particles, one can use an external magnetic field to apply force on the particles. The Monte-Carlo method provides a mesh-free approach to model the field of a permanent magnet even with a complex shape. Generally, using this method, any complex permanent magnet can be modeled as *NC* magnetic components, where the magnetization vector of each component can be defined in arbitrary magnitude and direction. Eq. (22) defines the magnetic field strength of the permanent magnet at an arbitrary point P as a summation of the effect of all combined components used to describe the permanent magnet:

$$H_m(p) = -\frac{1}{4\pi}\nabla \iiint \frac{(\vec{M}.\vec{r})}{|r^3|} dV \tag{22}$$

Defining the arbitrary magnetization vector $M = [M_x\ M_y\ M_z]$ and position vector $r = [x\ y\ z]$ (which represents the distance of a magnetic component to an arbitrary point Γ), one can obtain the components of $H_m(p)$ along the x, y, and z directions, as shown in Eqs. (23)–(25):

$$H_{mx}(p) = \frac{-dV}{4\pi}\left[\frac{M_x}{(r)^3} - \frac{3x(M_x x + M_y y + M_z z)}{(r)^5}\right] \tag{23}$$

$$H_{my}(p) = \frac{-dV}{4\pi}\left[\frac{M_y}{(r)^3} - \frac{3y(M_x x + M_y y + M_z z)}{(r)^5}\right] \tag{24}$$

$$H_{mz}(p) = \frac{-dV}{4\pi}\left[\frac{M_z}{(r)^3} - \frac{3z(M_x x + M_y y + M_z z)}{(r)^5}\right] \tag{25}$$

Superposition of the magnetic field strength H of all magnetic components $p = 1\ to\ NC$ with volume dV on an arbitrary point Γ defines the magnetic field effect of the permanent magnet at point Γ. Using Eqs. (23)–(25), one can calculate H on each ferromagnetic particle in the particle bed. With H, one can calculate the magnetic flux density B due to the permanent magnet on each particle in the particle bed. To calculate the force acting on the ferromagnetic particles due to the external magnetic field, Eq. (26) is used, where μ_0 is the permeability of vacuum, B is the magnetic flux density in Tesla, and A is the area of the particle in m^2 :

$$F = \frac{B^2 A}{2\mu_0} \tag{26}$$

3. Experiment setup

Fig. 3 shows the setup used to measure temperature distribution in a particle bed domain. The setup is made of a glass container sealed by an aluminum plate at the bottom and a phenolic plate on top. The diameter of the container is 5 cm, and its total height, including gaskets, is 10.8 cm. A circular ultra-thin heat sheet with a maximum power of 31 *W* is attached below the aluminum plate. Three thermocouples are used to read the temperature inside the container: one in direct contact with the aluminum plate, the second and third are 1 *cm* and 2 *cm* above the bottom plate, respectively. All three thermocouples are aligned at the center of the container. Power supplied to the heater is 1.8 *W* (30 *V*, 0.06 *A*), and the maximum magnetic flux is 990 *G* for the experiment under a magnetic field. The external magnetic field is provided by a disc NdFeB permanent magnet with a radius of 25 mm and a thickness of 9.5 mm. The initial temperature of the setup was recorded for two minutes, and then heating started. The heating process continued for approximately two hours. The container was filled with 542.936 grams of iron powder with a particle size of $150 - 300\ \mu m$. To get distribution of particle sizes as close as possible to uniform distribution, particles are sieved using available sieve sizes [149-177], [177-210], [210-250] and [250-297] μm and mixed after with %18, %22, %27 and %33 weight ratio, respectively. To have the same boundary conditions and thermal loads for both cases with and without magnetic field, an identical disc magnet was demagnetized and used in the experiment without magnetic field. This adds similar thermal resistance to the setup for both cases. Finally, it should be mentioned that the experimental setup is kept in a temperature-controlled environment to make sure the initial temperature is equal for both magnetic and non-magnetic cases before starting the heating process.

4. Simulation results and verification

A simulation of heat transfer in the particle bed shown in Fig. 3 using methods that require the composition of all particles to be precisely defined uses more than six million particles to set the geometry. It is therefore very time and memory consuming to solve this problem using either FEM or DEM methods. Using the proposed method, Eqs. (20) and (21) show that the length of the energy transfer path is a function of the time step τ. Therefore, the total number of required points to set up the geometry should be large enough so that the distance between points is smaller than the energy transfer path, and subsequently, accurate interpolation can be performed. 20 thousand particles used to randomly fill the

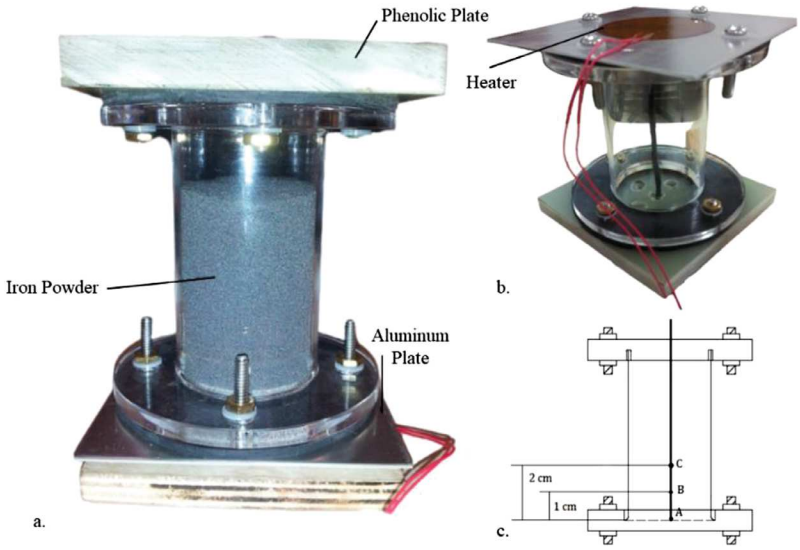

Fig. 3. Experimental setup for heat transfer measurements in particulate packed bed. (a). Filled container, (b). reversed empty container and heater, (c). Location of thermocouples A, B and C.

Table 2
Material properties of solid particles.

Density-ρ	Thermal Conductivity-k	Heat Capacity-C_p	Hardness Brinell -H_B	Elastic Modulus-E	Poisson's Ratio-ν	Surface Roughness-σ
7850 $[\frac{kg}{m^3}]$	37 $[\frac{W}{m-K}]$	456 $[\frac{J}{kg-K}]$	4.5 $[GPa]$	165 $[GPa]$	0.3	$1-5$ $[\mu m]$

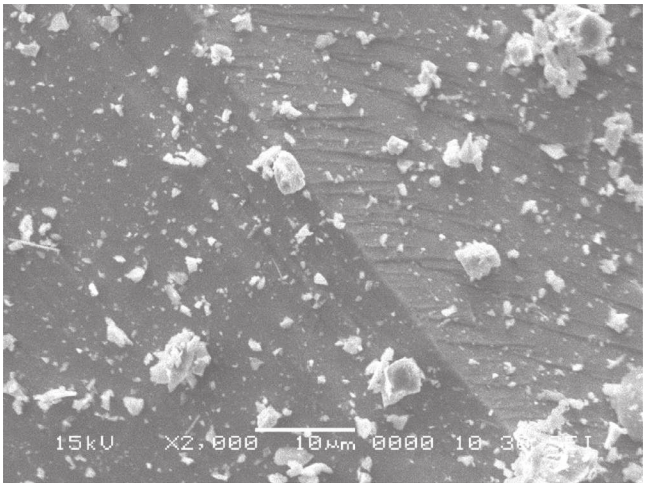

Fig. 4. Scanning electron microscopy (SEM) of particles used in experiment, magnification X2000.

container volume and define the geometry are therefore sufficient. Table 2 shows the material properties of the iron powder used in the simulation. The values for material properties are obtained from literature [45–48]. The Fig. 4 shows scanning electron microscopy (SEM) with x2000 magnification to justify the scale used for the roughness.

The reading from thermocouple A in the experiment (Fig. 3) is fed to the points at the bottom boundary of the container in the simulation. The time step $\tau = 10\ s$ is chosen for a total simulation time of 7000 s to match the experiment. The size of the iron powder particles in the simulation are generated in a uniformly distributed range of 150 $\mu m < r_{(x,y,z)} < 300\ \mu m$ to match that of the experiment. Fig. 5 shows five different possible configurations for 130 energy transfer paths from probable sources to the sink in the center (local packed elements). 50 cases of these local packed elements were used in this simulation, and only five of them are shown here. Each energy transfer path is built as a chain of particles, with the cut off criterion of achieving a time to travel from thermal source to sink close to the time step $\tau = 10\ s$.

A random number between 1 to 50 is generated before calculation of the temperature distribution at each particle in the domain, and the respective configuration case is employed for that purpose. This helps in reaching a more homogenous distribution of sources for the entire simulation.

For thermal resistance calculations, the force F acting on the particles is required. When the magnetic field does not exist, the weight of the particle and of the column of particles on top of it is calculated as the applied force F. For the case with an external magnetic field, Eqs. (23)–(25) are used to obtain the total magnetic field acting on each particle, and the resulting magnetic force is calculated using Eq. (26). The magnetization vector M is obtained from the H-B curve of the permanent magnet material when the remnant field B_r is considered 0.1 Tesla for NdFeB magnet. The mutual effects of magnetization among ferromagnetic particles in the domain are neglected in this study.

Fig. 6 shows the simulated magnetic flux density calculated with the proposed method compared to the one measured in the experiment. The disc magnet with a radius of 50 mm and a thickness of 9.8 mm is shown in black in all subplots. Fig. 6a shows the magnetic field lines around the magnet. The magnetic field measurements are done using a fluxgate at different radial and elevation locations on top of the disc magnet. Fig. 6b depicts the measurement point locations for magnetic field measurements. Fig. 6c and d show the magnetic flux density on the particle bed domain interpolated from measurement data and calculated from simulation, respectively.

Table 3
Thermal conductivity ratio for magnetic and non-magnetic cases.

Experimental	Simulation
$k_{ratio} = 1.127$ *or* 12.7%	$k_{ratio} = 1.098$ *or* 9.8%

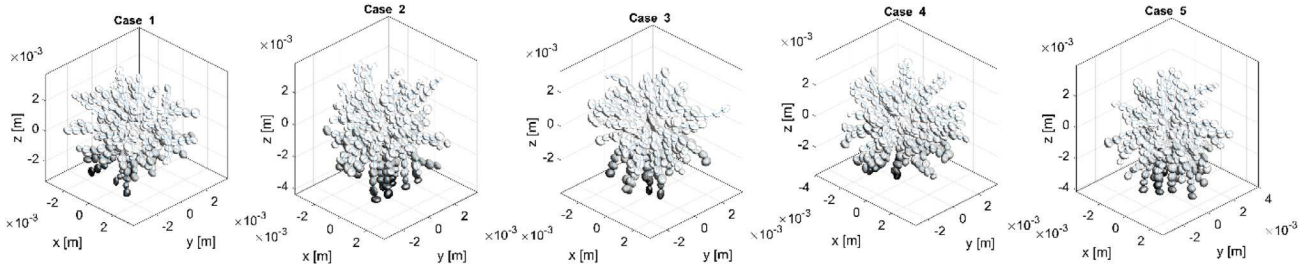

Fig. 5. Five energy transfer path configurations (local packed elements) for time step $\tau = 10$ *s*.

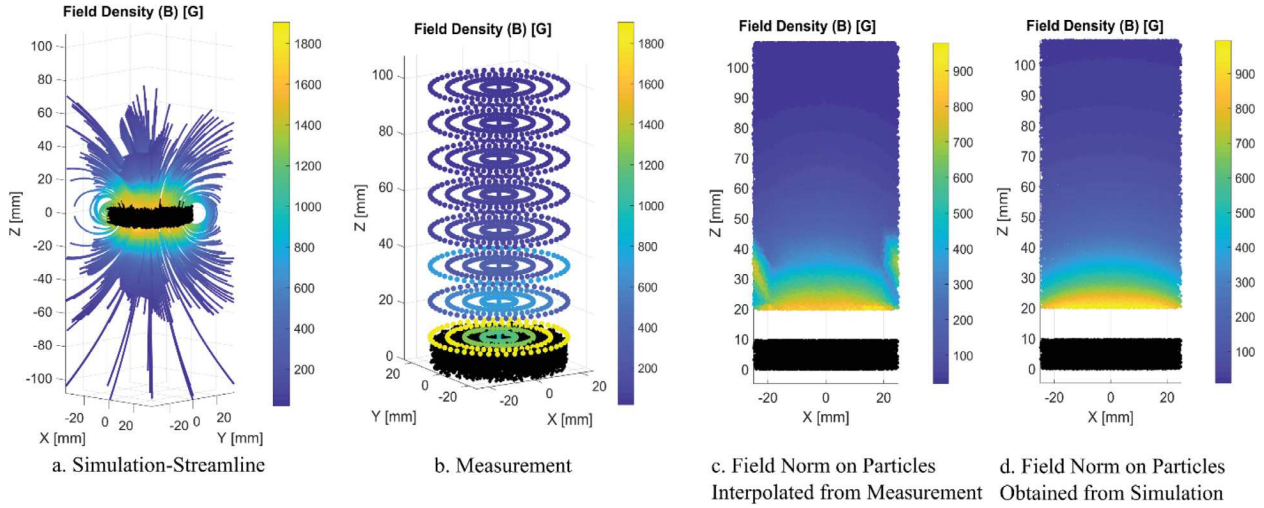

Fig. 6. Magnetic Flux Density- Simulations and measurements. 5.a: magnetic field lines around the magnet, 5.b: measurement point locations for magnetic field measurements. 5.c: magnetic flux density on the particle bed domain interpolated from measurement data, 5.d: magnetic flux density on the particle bed domain calculated from simulation

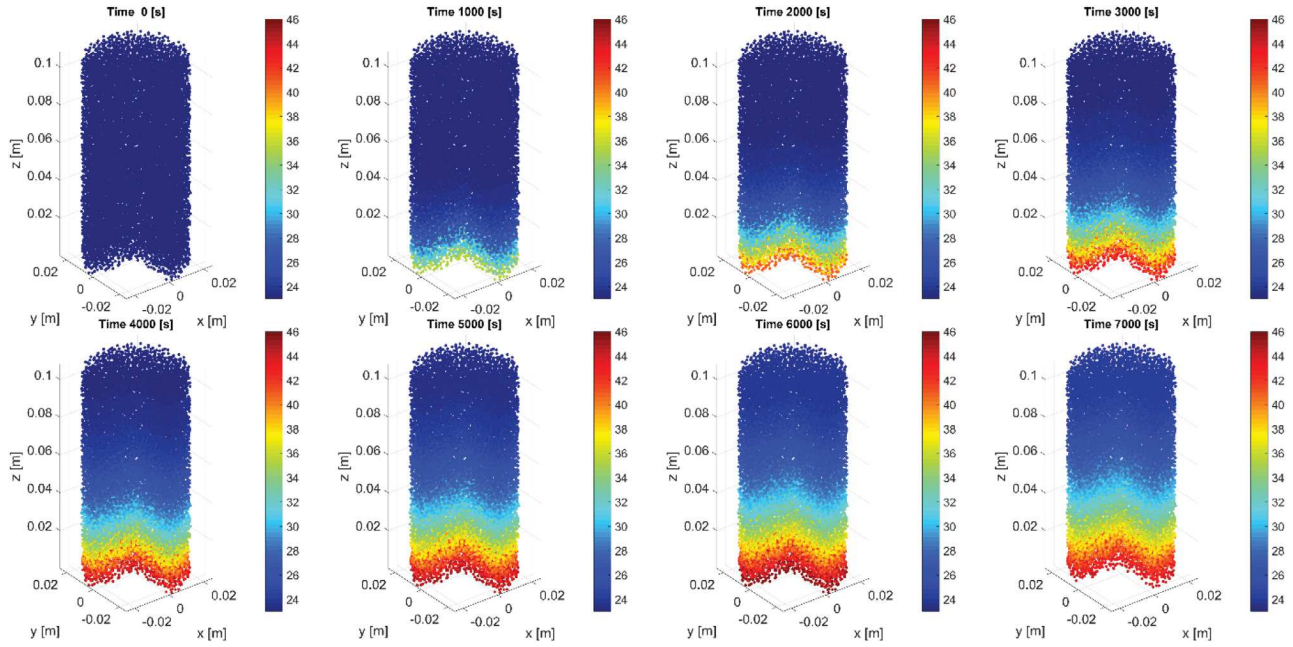

Fig. 7. Simulation results for non-magnetic temperature distribution in particulate bed domain with 1000 s time interval.

Fig. 7 shows the temperature distribution for a non-magnetic case at a time interval of 1000 *s* from initial time 0 *s* to final simulation time 7000 *s*. A quarter slice of the pack bed is removed to show the radial temperature distribution. To allow quantitative comparison and benchmark of the proposed method, the simulation results of temperature rise at the exact locations of thermocouples B and C (10 *mm* and 20 *mm* from the bottom of the container) are captured and compared with measurement data for both the magnetic and non-magnetic cases and shown in Fig. 8. The results are in an excellent agreement with the experimental measurements. Both theoretical and empirical results show an increase in the thermal conductivity of the domain. The increase is

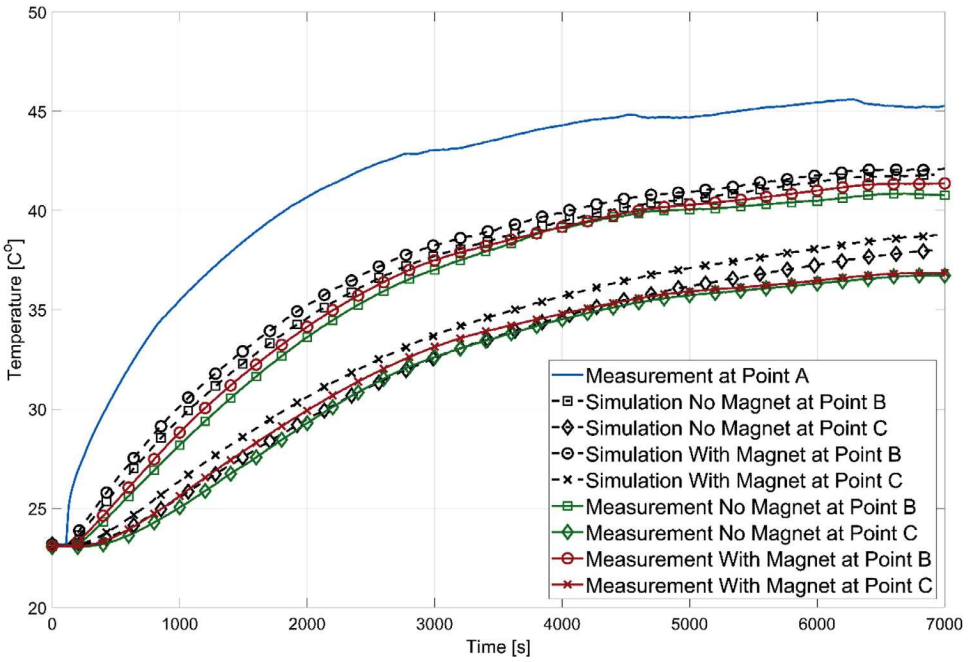

Fig. 8. Simulation versus measurement for temperature distribution at thermocouples A and B locations for magnetic and non-magnetic cases.

calculated using Eq. (27) [49] and shown in Table 3.

$$k_{ratio} = \frac{k_{Magnetic}}{k_{Non-Magnetic}} = \frac{(T_B - T_A)_{Non-Magnetic}}{(T_B - T_A)_{Magnetic}} \tag{27}$$

where T_A and T_B are the temperatures at the location of thermocouples A and B at the steady-state condition, respectively.

5. Conclusions

The proposed method provides a probabilistic approach to solve the conductive heat transfer problem in particulate materials with no requirement of mesh generation or knowing the exact location of all particles. It provides a parallelizable method that can achieve a significant reduction in both simulation time and memory requirements in these kinds of problems compared to conventional FEM, DEM and FDM methods. Besides requiring a significantly smaller number of particles (compared to conventional FEM, DEM and FDM) the proposed mesh free Monte Carlo approach enables parallel solution of the heat transfer for each particle to be assigned to an individual core on a GPU platform, further enabling a reduction of simulation time that can be several orders of magnitude smaller compared to conventional FEM solutions.

Simulated results obtained with the proposed mesh-free Monte Carlo approach show good agreement with experimental results, for both the prediction of magnetic field density in the 3D domain, as well as for the prediction of conductive heat transfer in both magnetic and non-magnetic cases.

It is shown that the presence of an external magnetic field increases thermal conductivity in ferromagnetic particulate materials due to the magnetic forces acting in the particles. Although the effect of gas thermal resistance in micro and macro gaps was neglected, it did not affect considerably the accuracy of the simulated results, since the corresponding passive convection has a marginal effect on heat transfer.

It is once again confirmed that probabilistic methods are good candidates to simulate boundary and initial value problems where physical parameters follow random distributions. The effect of forced convection, radiation at high temperature, and even phase change (for the cases when melting and solidification of particles happen such as Laser Powder Bed Fusion) can be considered in the future development of the proposed method.

Declaration of Competing Interest

We wish to confirm that there are no known conflicts of interest associated with this publication and there has been no significant financial support for this work that could have influenced its outcome. We confirm that the manuscript has been read and approved by all named authors and that there are no other persons who satisfied the criteria for authorship but are not listed. We further confirm that the order of authors listed in the manuscript has been approved by all of us. We confirm that we have given due consideration to the protection of intellectual property associated with this work and that there are no impediments to publication, including the timing of publication, with respect to intellectual property. In so doing we confirm that we have followed the regulations of our institutions concerning intellectual property. We understand that the Corresponding Author is the sole contact for the Editorial process (including Editorial Manager and direct communications with the office). He/she is responsible for communicating with the other authors about progress, submissions of revisions and final approval of proofs. We confirm that we have provided a current, correct email address which is accessible by the Corresponding Author and which has been configured to accept email from (rbahadori2013@my.fit.edu)

CRediT authorship contribution statement

Reza Bahadori: Writing – original draft, Formal analysis, Writing – review & editing, Conceptualization, Methodology. **Hector Gutierrez:** Supervision, Writing – review & editing, Resources, Funding acquisition. **Shahin Shafiee:** Writing – review & editing, Validation.

Acknowledgment

This work is supported by the National Science Foundation [1827730, 2018].

References

[1] M. Hirata, T. Gotou, M. Ohba, Thin-film particles of graphite oxide. 2: preliminary studies for internal micro fabrication of single particle and carbonaceous electronic circuits, Carbon N. Y. 43 (3) (2005) 503–510, doi:10.1016/j.carbon.2004.10.009.

[2] W.-H. Lee, Y. Zhang, J. Zhang, Discrete element modeling of powder flow and laser heating in direct metal laser sintering process, Powder Technol. 315 (2017) 300–308 Jun., doi:10.1016/j.powtec.2017.04.002.

[3] S.K. Rauniyar, K. Chou, Melt pool analysis and mesoscale simulation of laser powder bed fusion process (L-PBF) with Ti-6Al-4V powder particles, JOM 71 (3) (2019) 938–945 Mar., doi:10.1007/s11837-018-3208-2.

[4] F.K. Mirzade, A.V. Dubrov, V.D. Dubrov, On numerical modeling of heat transfer and fluid flow in selective laser melting of metal powder bed, in: 3D Printed Optics and Additive Photonic Manufacturing, 10675, 2018, p. 38, doi:10.1117/12.2307530. May.

[5] Y. Huang, L.J. Yang, X.Z. Du, Y.P. Yang, Finite element analysis of thermal behavior of metal powder during selective laser melting, Int. J. Therm. Sci. 104 (2016) 146–157 Jun., doi:10.1016/j.ijthermalsci.2016.01.007.

[6] A. Yahya, R. Rabhi, H. Dhahri, K. Slimi, Numerical simulation of temperature distribution in a planar solid oxide fuel cell using lattice Boltzmann method, Powder Technol 338 (2018) 402–415 Oct., doi:10.1016/j.powtec.2018.07.060.

[7] B. Zheng, et al., Study on heating performances of steam generator for solid oxide fuel cell using waste heat from solid particles, Int. J. Hydrogen Energy 44 (46) (2019) 25221–25228 Sep., doi:10.1016/j.ijhydene.2019.03.020.

[8] G. Mauer, Numerical study on particle-gas interaction close to the substrates in thermal spray processes with high-kinetic and low-pressure conditions, J. Therm. Spray Tech. 28 (2019) 27–39, doi:10.1007/s11666-018-0810-3.

[9] Y. Cui, et al., Porous nanostructured ZrO_2 coatings prepared by plasma spraying, Surf. Coat. Technol. 363 (2019) 112–119 Apr., doi:10.1016/j.surfcoat.2019.02.059.

[10] G. Boissonnet, G. Bonnet, A. Pasquet, N. Bourhila, F. Pedraza, Evolution of thermal insulation of plasma-sprayed thermal barrier coating systems with exposure to high temperature, J. Eur. Ceram. Soc. 39 (6) (2019) 2111–2121 Jun., doi:10.1016/J.JEURCERAMSOC.2019.01.026.

[11] P. Bartsch, S. Zunft, Granular flow around the horizontal tubes of a particle heat exchanger: DEM-simulation and experimental validation, Sol. Energy 182 (2019) 48–56 Apr., doi:10.1016/j.solener.2019.01.086.

[12] J.A. Shamim, S. Paul, W.-L. Hsu, K. Kitaoka, H. Daiguji, Theoretical analysis of transient heat and mass transfer during regeneration in multilayer fixed-bed binder-free desiccant dehumidifier: model validation and parametric study, Int. J. Heat Mass Transf. 134 (2019) 1024–1040 May, doi:10.1016/j.ijheatmasstransfer.2019.01.094.

[13] S. Shafiee, M.H. McCay, Different reactor and heat exchanger configurations for metal hydride hydrogen storage systems - a review, Int. J. Hydrogen Energy 41 (22) (2016) 9462–9470, doi:10.1016/j.ijhydene.2016.03.133.

[14] S. Shafiee, Operational principles and effect of operating parameters on performance of metal hydride heat pumps, Int. J. Refrig. (2020) 22–30 Aug., doi:10.1016/j.ijrefrig.2020.08.025.

[15] H. Ludewig, J.R. Powell, M. Todosow, G. Maise, R. Barletta, D.G. Schweitzer, Design of particle bed reactors for the space nuclear thermal propulsion program, Prog. Nucl. Energy 30 (1) (1996) 1–65, doi:10.1016/0149-1970(95)00080-4.

[16] F.R. Liu, Q. Zhang, W.P. Zhou, J.J. Zhao, J.M. Chen, Micro scale 3D FEM simulation on thermal evolution within the porous structure in selective laser sintering, J. Mater. Process. Technol. 212 (10) (2012) 2058–2065 Oct., doi:10.1016/J.JMATPROTEC.2012.05.010.

[17] G.A. Narsilio, J. Kress, T.S. Yun, Characterisation of conduction phenomena in soils at the particle-scale: finite element analyses in conjunction with synthetic 3D imaging, Comput. Geotech. 37 (7–8) (2010) 828–836 Nov., doi:10.1016/J.COMPGEO.2010.07.002.

[18] J.H. Zhou, A.B. Yu, M. Horio, Finite element modeling of the transient heat conduction between colliding particles, Chem. Eng. J. 139 (3) (2008) 510–516 Jun., doi:10.1016/j.cej.2007.08.024.

[19] L. Qian, X. Pang, J. Zhou, J. Yang, S. Lin, D. Hui, Theoretical model and finite element simulation on the effective thermal conductivity of particulate composite materials, Compos. Part B Eng. 116 (2017) 291–297, doi:10.1016/j.compositesb.2016.10.067.

[20] Z. Luo, Y. Zhao, A survey of finite element analysis of temperature and thermal stress fields in powder bed fusion, Addit. Manuf. 21 (2018) 318–332 May, doi:10.1016/J.ADDMA.2018.03.022.

[21] M. Bahrami, M.M. Yovanovich, J.R. Culham, Effective thermal conductivity of rough spherical packed beds, Int. J. Heat Mass Transf. 49 (19–20) (2006) 3691–3701 Sep., doi:10.1016/j.ijheatmasstransfer.2006.02.021.

[22] I.A. Roberts, C.J. Wang, R. Esterlein, M. Stanford, D.J. Mynors, A three-dimensional finite element analysis of the temperature field during laser melting of metal powders in additive layer manufacturing, Int. J. Mach. Tools Manuf. 49 (12–13) (2009) 916–923 Oct., doi:10.1016/J.IJMACHTOOLS.2009.07.004.

[23] Y. Asakuma, S. Miyauchi, T. Yamamoto, H. Aoki, T. Miura, Homogenization method for effective thermal conductivity of metal hydride bed, Int. J. Hydrogen Energy 29 (2) (2004) 209–216 Feb., doi:10.1016/S0360-3199(03)00106-X.

[24] J. Romano, L. Ladani, M. Sadowski, Thermal modeling of laser based additive manufacturing processes within common materials, Proc. Manuf. 1 (2015) 238–250, doi:10.1016/j.promfg.2015.09.012.

[25] M. Bonnet, Boundary Integral Equation Methods for Solids and Fluids, J. Wiley, 1995.

[26] J. Zhou, A. Yu, Y. Zhang, A boundary element method for evaluation of the effective thermal conductivity of packed beds, J. Heat Transf. 129 (3) (2007) 363–371 Mar., doi:10.1115/1.2430721.

[27] C.A. Brebbia, J. Dominquez, Boundary Elements : an Introductory Course, Computational Mechanics Publications, 1992.

[28] J. Polansky, N. Jeffers, J. Punch, A hybrid approach for predicting the effective thermal conductivity of sintered porous materials, Int. J. Therm. Sci. 148 (2020) 106135 Feb., doi:10.1016/j.ijthermalsci.2019.106135.

[29] H. Xin, W. Sun, J. Fish, Discrete element simulations of powder-bed sintering-based additive manufacturing, Int. J. Mech. Sci. 149 (2018) 373–392 Dec., doi:10.1016/j.ijmecsci.2017.11.028.

[30] H. Wu, N. Gui, X. Yang, J. Tu, S. Jiang, A smoothed void fraction method for CFD-DEM simulation of packed pebble beds with particle thermal radiation, Int. J. Heat Mass Transf. 118 (2018) 275–288 Mar., doi:10.1016/J.IJHEATMASSTRANSFER.2017.10.123.

[31] M. Moscardini, Y. Gan, S. Pupeschi, M. Kamlah, Discrete element method for effective thermal conductivity of packed pebbles accounting for the Smoluchowski effect, Fusion Eng. Des. 127 (2018) 192–201 Feb., doi:10.1016/J.FUSENGDES.2018.01.013.

[32] E. Tsotsas, Particle-particle heat transfer in thermal DEM: three competing models and a new equation, Int. J. Heat Mass Transf. 132 (2019) 939–943 Apr., doi:10.1016/J.IJHEATMASSTRANSFER.2018.12.090.

[33] M. Baniasadi, M. Baniasadi, B. Peters, Coupled CFD-DEM with heat and mass transfer to investigate the melting of a granular packed bed, Chem. Eng. Sci. 178 (2018) 136–145 Mar., doi:10.1016/j.ces.2017.12.044.

[34] A.R. Peeketi, M. Moscardini, A. Vijayan, Y. Gan, M. Kamlah, R.K. Annabattula, Effective thermal conductivity of a compacted pebble bed in a stagnant gaseous environment: an analytical approach together with DEM, Fusion Eng. Des. 130 (2018) 80–88 May, doi:10.1016/J.FUSENGDES.2018.02.088.

[35] V. García-García, I. Mejía, F. Reyes-Calderón, Two-dimensional Monte Carlo–Voronoi simulation of grain growth and nucleation in the heat affected zone of TWIP-Ti welds, Materialia 5 (2019) 100223 Mar., doi:10.1016/j.mtla.2019.100223.

[36] L. Ju, Q. Du, M. Gunzburger, Probabilistic methods for centroidal Voronoi tessellations and their parallel implementations, Parallel Comput. 28 (10) (2002) 1477–1500 Oct., doi:10.1016/S0167-8191(02)00151-5.

[37] I.C. Kim, An efficient Brownian motion simulation method for the conductivity of a digitized composite medium, KSME Int. J. 17 (4) (2003) 545–561, doi:10.1007/BF02984456.

[38] M.M. Tomadakis, S.V. Sotirchos, Effective diffusivities and conductivities of random dispersions of nonoverlapping and partially overlapping unidirectional fibers, J. Chem. Phys. 99 (12) (1993) 9820–9827 Dec., doi:10.1063/1.465464.

[39] A. Haji-Sheikh, E.M. Sparrow, The floating random walk and its application to Monte Carlo solutions of heat equations, SIAM J. Appl. Math. 14 (2) (1966) 370–389.

[40] R. Bahadori, H. Gutierrez, S. Manikonda, R. Meinke, Two-dimensional transient heat conduction in multi-layered composite media with temperature dependent thermal diffusivity using floating random walk Monte-Carlo method, Int. J. Heat Mass Transf. 115 (2017) 570–580 Dec., doi:10.1016/j.ijheatmasstransfer.2017.07.071.

[41] R. Bahadori, H. Gutierrez, S. Manikonda, R. Meinke, A mesh-free Monte-Carlo method for simulation of three-dimensional transient heat conduction in a composite layered material with temperature dependent thermal properties, Int. J. Heat Mass Transf. 119 (2018) 533–541, doi:10.1016/j.ijheatmasstransfer.2017.11.140.

[42] R. Bahadori, H. Gutierrez, Effective floating volume: a highly parallelizable mesh-free approach for solving transient multiphysics problems in multi-scale geometries with non-linear material properties, Comput. Mech. 65 (3) (2020) 839–852 Mar., doi:10.1007/s00466-019-01797-x.

[43] J. Mo, H. Ban, Measurements and theoretical modeling of effective thermal conductivity of particle beds under compression in air and vacuum, Case Stud. Therm. Eng. 10 (2017) 423–433 Sep., doi:10.1016/j.csite.2017.10.001.

[44] M. Bahrami, J.R. Culham, M.M. Yovanovich, Modeling thermal contact resistance: a scale analysis approach, J. Heat Transf. 126 (6) (2004) 896–905 Dec., doi:10.1115/1.1795238.

[45] H.-K. Mao, T. Takahashi, W.A. Bassett, G.L. Kinsland, L. Merrill, Isothermal compression of magnetite to 320 KB, J. Geophys. Res. 79 (8) (1974) 1165–1170 Mar., doi:10.1029/jb079i008p01165.

[46] C.L. Snow, Q. Shi, J. Boerio-Goates, B.F. Woodfield, Heat capacity studies of nanocrystalline magnetite (Fe_3O_4), J. Phys. Chem. C 114 (49) (2010) 21100–21108 Dec., doi:10.1021/jp1072704.

[47] E.F. Westrum, F. Grønvold, Magnetite (Fe_3O_4) heat capacity and thermodynamic properties from 5 to 350 K, low-temperature transition, J. Chem. Thermodyn. 1 (6) (1969) 543–557 Nov., doi:10.1016/0021-9614(69)90015-9.

[48] J. Mølgaard, W.W. Smeltzer, Thermal conductivity of magnetite and hematite, J. Appl. Phys. 42 (9) (1971) 3644–3647 Aug., doi:10.1063/1.1660785.

[49] S. Shafiee, M.H. McCay, S. Kuravi, Effect of magnetic fields on thermal conductivity in a ferromagnetic packed bed, Exp. Therm. Fluid Sci. 86 (2017) 160–167, doi:10.1016/j.expthermflusci.2017.04.014.